Anisotropy of Surfzone Turbulence

JINSHI CHEN,[a,b] BRITT RAUBENHEIMER,[c] AND STEVE ELGAR[c]

[a] *Physical Oceanography, Woods Hole Oceanographic Institution, Woods Hole, Massachusetts*
[b] *Department of Earth, Atmospheric, and Planetary Sciences, Massachusetts Institute of Technology, Cambridge, Massachusetts*
[c] *Applied Ocean Physics & Engineering, Woods Hole Oceanographic Institution, Woods Hole, Massachusetts*

(Manuscript received 10 September 2024, in final form 9 May 2025, accepted 28 May 2025)

ABSTRACT: Turbulent anisotropy was estimated using two vertically stacked acoustic Doppler velocimeters (ADVs) deployed in the surfzone (2-m mean water depth) for 18 days with offshore wave heights ranging from 0.8 to 5.7 m. Consistent with prior observations, $[c_t]$, a depth-averaged parameter for cross-shore vertical [two dimensional (2D)] anisotropy, is greater than 1, which is larger than the suggested value (0.22) based on plane wake turbulence. The estimated 2D anisotropy increases weakly from the inner to the outer surfzone (with an increasing ratio of local to offshore wave energy flux) and decreases weakly with vertical shear of the cross-shore current. Only near-surface 2D anisotropy is correlated weakly with wave directional spread, suggesting that the processes affecting anisotropy are depth-dependent. At low frequencies ($f < 0.05$ Hz), 2D anisotropy is larger than that in the higher-frequency inertial subrange and decreases toward the seafloor and with increasing vertical shear of the cross-shore current, approaching that for wave–current bottom-boundary-layer turbulence when the vertical shear is large. The three-dimensional turbulence Reynolds stress tensor is related to the total vertical current shear, as well as to the directions of both mean currents and waves. Horizontal turbulence length scales are larger than the vertical length scales, consistent with previous studies.

KEYWORDS: Turbulence; Wave breaking; In situ oceanic observations

1. Introduction

Breaking-wave-generated turbulence is essential to momentum diffusion and energy dissipation in the surfzone (Feddersen 2012; Chen et al. 2024b), enhancing sediment transport (Nadaoka et al. 1988; Aagaard and Hughes 2010), and bottom drag (Apotsos et al. 2007). In the surfzone, turbulence dissipates incoming wave energy, limiting wave heights in shallow water (Chen et al. 2024b). In the vertical, turbulence shear stresses redistribute the momentum in the water column, shaping the vertical structure of the offshore directed current (undertow) beneath the wave trough (Svendsen 1984; De Vriend and Stive 1987; Deigaard and Fredsøe 1989; Boers 2005). When breaking-wave-generated turbulence reaches the bed, enhanced bottom friction may contribute to setup, the increase in the mean sea level owing to breaking waves (Apotsos et al. 2007).

Previous studies of surfzone turbulence have focused on the dissipation rate, length scale, and magnitude of shear stresses (Boers 2005; Feddersen and Williams 2007; Feddersen 2012). However, few studies exist of the surfzone turbulence Reynolds stress tensor, including the directional dependence of the normal stresses and deviations from an isotropic state (the turbulent anisotropy; Biferale and Procaccia 2005; Thomson et al. 2012), which affects momentum flux transfers and turbulent mixing (Roelvink and Stive 1989; Mellor and Yamada 1982; Biferale and Procaccia 2005; Mellor 2013). Improved understanding of turbulent anisotropy is needed to improve parameterizations of the three-dimensional (3D) turbulence in models.

For example, the two-dimensional (2D, cross-shore vertical) turbulent anisotropy affects the turbulent radiation stress $S_{xx,\text{turbulence}}$, which contributes to the cross-shore momentum equation similar to wave radiation stress (Roelvink and Stive 1989; Chen et al. 2024b):

$$S_{xx,\text{turbulence}} \approx \rho \overline{\int_{-h}^{\eta} (u'^2 - w'^2) dz}, \tag{1}$$

where ρ is the water density, h is the seafloor depth below mean water level, η is the instantaneous water level, u' and w' are the cross-shore and vertical turbulent velocity fluctuations, respectively, z is the vertical coordinate, and the overbar indicates a time average. The turbulence radiation stress has been parameterized as (Roelvink and Stive 1989; Nairn et al. 1990; Chen et al. 2024b)

$$S_{xx,\text{turbulence}} \approx [c_t]\rho[\overline{k_{2D}}]h, \tag{2}$$

where [] indicates a depth average and $c_t(z)$ is the depth-resolved parameter for 2D anisotropy defined as

$$c_t(z) = 2\frac{\overline{u'^2} - \overline{w'^2}}{\overline{u'^2} + \overline{w'^2}}, \tag{3}$$

and $[c_t]$ is therefore a depth-averaged constant parameter. The time- and depth-averaged cross-shore and vertical turbulent kinetic energy (TKE) $[\overline{k_{2D}}]$ is defined as

$$[\overline{k_{2D}}] = \frac{1}{h + \overline{\eta}} \overline{\int_{-h}^{\eta} \frac{u'^2 + w'^2}{2} dz}. \tag{4}$$

The choice of $[c_t]$ determines the relative importance of turbulence radiation stress to other mechanisms (e.g., roller,

Corresponding author: Jinshi Chen, jinshic@mit.edu

DOI: 10.1175/JPO-D-24-0177.1

bottom stress) that transfer momentum flux from the breaking wave to the water column (Chen et al. 2024b). However, there is no consensus on the value of $[c_t]$, and the dependence of $[c_t]$ on bulk wave and current properties is uncertain. Assuming that surfzone turbulence resembles plane wake turbulence, $[c_t] \approx 0.22$ (Tennekes and Lumley 1972; Svendsen 1987). Limited field measurements (Ruessink 2010) suggest that $[c_t]$ may be larger, and numerical simulations of cross-shore wave transformation (Chen et al. 2024b) require $[c_t] \approx 1$ to close the momentum budget and suggest that turbulence accounts for about 20% of the momentum flux transferred from breaking waves. In wave flume experiments, the ratio of $\overline{u_i'^2}$ to $\overline{w_i'^2}$ increases toward the bed where it can be as large as 5, indicating the local $c_t(z)$ is ≈ 1.33 (Ting and Kirby 1996; Ruessink 2010). Both the ratio of $\overline{u'^2}$ to $\overline{w'^2}$ and the parameter $c_t(z)$ may be frequency dependent, with larger-scale, lower-frequency turbulence being more vertically confined (larger $\overline{u'^2}$ compared with $\overline{w'^2}$) than smaller-scale higher-frequency turbulence (Thomson et al. 2012). However, there are few field investigations of c_t.

In 3D, the relative importance r_k of alongshore normal stresses ($\overline{v'^2}$) compared with cross-shore ($\overline{u'^2}$) and vertical ($\overline{w'^2}$) normal stresses is given by (Stive and Wind 1982; Svendsen 1987; Larsen and Fuhrman 2018)

$$r_k(z) = \frac{\overline{u'^2} + \overline{v'^2} + \overline{w'^2}}{\overline{u'^2} + \overline{w'^2}}. \tag{5}$$

Two-dimensional (2D) TKE measured in narrow wave flumes and simulated in 2D models often is converted and compared with 3D TKE measured in the field or the laboratory using $r_k = 1.33$ (Ruessink 2010; Larsen and Fuhrman 2018; Larsen et al. 2020). In isotropic turbulence $r_k = 1.5$, and turbulent wakes, boundary layers, mixing layers, and plane jet flows have r_k between 1.3 and 1.4, which is the value commonly assumed for surfzone breaking waves (Svendsen 1987). However, recent laboratory and field studies suggest $r_k \sim 1.5$–1.6 in the surfzone (Scott et al. 2005; Ruessink 2010). In a large-scale flume experiment, r_k was similar to that for a plane wake near the surface but was closer to that expected for boundary layer flow near the bed (Yoon and Cox 2010).

Although these studies provide insights into the structure of normal stresses, the results depend on the alignment of waves, currents, and bathymetry contours, which vary with time and space on natural beaches. Coordinate-independent three-dimensional turbulence anisotropy and the orientation of turbulence can be estimated from the full three-dimensional normalized anisotropic tensor, which includes both normal and shear stresses (Pope 2000; Banerjee et al. 2007; McCaffrey et al. 2015):

$$b_{ij} = \frac{\overline{u_i'u_j'}}{2k} - \frac{1}{3}\delta_{ij}, \tag{6}$$

where b_{ij}, which indicates the (i, j) component of the tensor, is traceless and is nonzero only when the turbulence is anisotropic, $k = (1/2)\overline{u_i'u_i'}$ is 3D TKE, and δ_{ij} is the Kronecker delta. Although the anisotropic tensor has been used to understand Langmuir turbulence (Li and Fox-Kemper 2020), tidal channel flow (McCaffrey et al. 2015), and wind turbine wakes (Ali et al. 2018), it has not been examined in surfzone turbulence.

Anisotropic turbulence also affects the correlation and mixing length scales, which relate turbulent shear stresses to mean flow shear and are important to turbulent mixing in the surfzone (Tennekes and Lumley 1972; Mellor and Yamada 1982; Biferale and Procaccia 2005; Mellor 2013). Reynolds-averaged Navier–Stokes (RANS) models that use k–ϵ (Launder and Sharma 1974) or k–ω (Wilcox 2006) two-equation closures usually include the turbulence Boussinesq approximation (Boussinesq 1877), where the Reynolds stress τ_{ij} and ensemble flow strain-rate tensors S_{ij} are defined as

$$\tau_{ij} = \overline{u_i'u_j'} \quad S_{ij} = \frac{1}{2}\left(\frac{\partial U_i}{\partial x_j} + \frac{\partial U_j}{\partial x_i}\right), \tag{7}$$

where the ith component of the velocity fluctuations u_i', the ith component of the ensemble flow U_i, and the ith spatial coordinate x_i are related via (Boussinesq 1877)

$$\tau_{ij} = 2\nu_t S_{ij} - \frac{2}{3}k\delta_{ij}, \tag{8}$$

where ν_t is the eddy viscosity. In this parameterization, which assumes the maximum flux of turbulent energy across scales, all Reynolds stresses are related to the mean flow strain rate (Pope 2000; Ballouz and Ouellette 2018). However, prior studies suggest $c_t \neq 0$ in the x–z plane even when only du/dz is present in the mean current strain tensor (Pope 2000), and the efficiency of transferring turbulent energy across scales can be as low as ≈25% in the inertial subrange for isotropic turbulence (Ballouz and Ouellette 2018). Moreover, laboratory observations of the vertical structure of undertow under breaking waves are reproduced more accurately using the Reynolds stress model, which considers each Reynolds stress component independently and relaxes the constraint on the Reynolds stresses by the strain-rate tensor, than by closures that rely on the turbulence Boussinesq approximation (Larsen and Fuhrman 2018; Li et al. 2022). Thus, the Boussinesq approximation can lead to inaccurate turbulence predictions that affect the undertow. Field studies of the anisotropy of surfzone turbulence are needed to relate these results to waves and mean currents over natural bathymetry.

Here, field observations (section 2) are used to investigate the 2D and 3D total and frequency-dependent turbulent anisotropy under depth-limited breaking waves and their relationships to bulk wave and current properties (section 3). Estimated length scales, and the effects of sensor separation, wave bias, and wave filtering methods are discussed (section 4).

2. Field study

a. Observations

Water levels, waves, and flows were measured at 16 Hz in the east–north-up (ENU) coordinate system at the U.S. Army

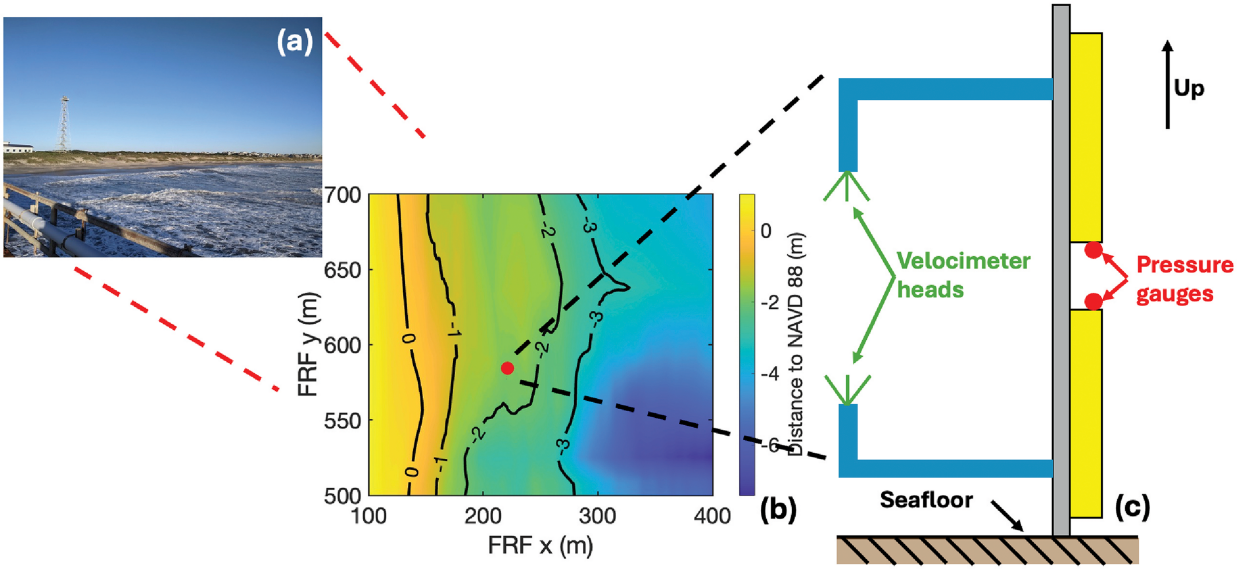

FIG. 1. (a) Photo of the field site looking shoreward from a pier; (b) depth contours relative to NAVD88 and the location of the stacked ADVs (red dot) as a function of alongshore and cross-shore coordinates on 25 Sep 2023; and (c) schematic of the stacked ADVs, including the pressure gauges (red circles) and velocimeters (sample volumes are 0.15 m from the central transducer where the three green arms meet) mounted on cantilevers (blue) attached to a vertical pipe (gray).

Corps of Engineers Field Research Facility (FRF) in Duck, North Carolina, between 19 September and 7 October 2023 with two vertically aligned acoustic Doppler velocimeters (ADVs) in roughly 2-m mean water depth (Fig. 1). Pressure gauges and velocity sample volumes on the two sensors were separated 0.31 and 0.32 m, respectively. The elevations of the sample volumes above the bed varied between about 0.45–0.77 and 0.69–1.01 m for the bottom and top ADV owing to erosion and accretion. Cantilevers (blue in Fig. 1c) holding the current meters (green in Fig. 1c) were oriented northeastward about 30° from shore parallel to minimize wake turbulence induced by the vertical pipe (gray in Fig. 1c) and sensor case (yellow in Fig. 1c). The smallest scale of turbulence that can be resolved is limited by the velocity sample volume, which is roughly a 0.010-m-tall, 0.015-m-diameter cylinder. The sensors were synced to an external GPS clock before deployment.

Significant wave heights H_s in 17-m water depth (not shown) ranged from 0.8 to 5.7 m, and the frequency of the peak of the spectrum ranged from 0.05 to 0.13 Hz, but typically was >0.07 Hz (not shown). Wave heights in 4.5-m water depth ranged from about 0.5 to 3.0 m [Fig. 2a, blue curve; U.S. Army Corps of Engineers (USACE) 2024] and typically were not breaking except between 23 and 24 September. In contrast, the ADV stack often was in the surfzone, and (tidal and surge) depth-modulated H_s ranged from 0.5 to 1.3 m (Fig. 2a, black curve) in water depths ranging from 1.4 to 2.8 m (not shown). Cross- and alongshore 30-min mean flows ($\overline{u}$ and $\overline{v}$, respectively) varied between 0.5 m s^{-1} onshore and offshore and 1.0 m s^{-1} northward to 0.8 m s^{-1} southward alongshore. The data used to investigate turbulence (Figs. 2a,b, small filled circles) span nearly the full range of mean flows but are dominated by conditions with alongshore flows less than 0.5 m s^{-1}. Wave directional spreads s_w estimated from cross-spectra between velocity components (Kuik et al. 1988) initially are small but increase to about 40° after 28

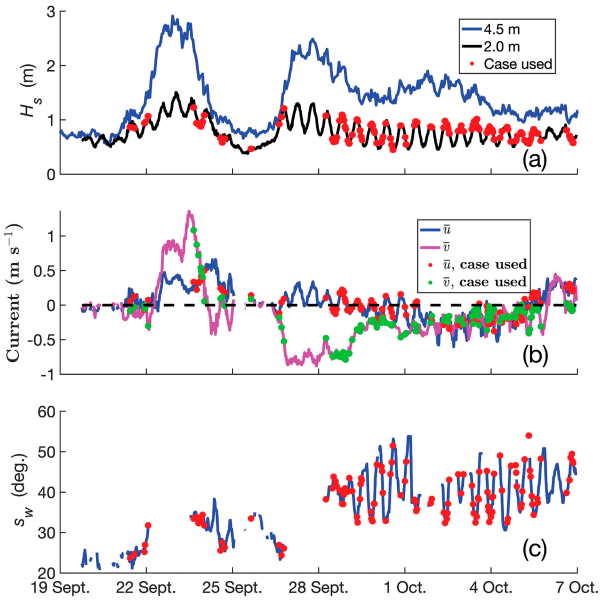

FIG. 2. (a) Significant wave height (H_s) in 4.5- (blue curve) and 2.0-m (black curve) mean water depths, (b) cross- ($\overline{u}$, blue) and alongshore ($\overline{v}$, magenta) mean currents (positive offshore and northward), and (c) wave directional spread s_w (including reflected waves) at the bottom ADV in 2-m water depth vs time (day month in 2023). Red and green circles in (a)–(c) indicate times that data passed quality control procedures for turbulence estimates.

September (Fig. 2c), at least partly owing to increased wave reflection from the sandbar, trough, and beach.

b. Data processing and quality control

Pressure and velocity data are separated into 30-min blocks (28 800 pts), and velocities are rotated to local alongshore and cross-shore directions (7° west and 83° east of magnetic north, respectively; Chen et al. 2024a). The data from the ADVs are time-synced using the lag giving the maximum correlation between the pressure time series. Maximum correlations were larger than 0.93 and usually larger than 0.97. The lag for the maximum correlation increased throughout the deployment from zero to about 1.8 s when the sensors were recovered.

Quality control of the velocity data included signal strength, signal correlation, and despiking tests. Time series with more than 0.8% of data points (230 pts) having signal-to-noise ratio (SNR) below 60 dB (indicating insufficient background scattering, possibly owing to the sensor being fouled or coming out of the water) were excluded from the analysis (Elgar et al. 2005; Feddersen 2010). Similar to prior studies, a correlation threshold of $0.3 + 0.4 \times \sqrt{F_s/25}$, where F_s is the sampling frequency (Elgar et al. 2001, 2005; 0.62 for 16-Hz sampling) is used to identify poor-quality data owing to excessive scattering of the acoustic signal, as may occur owing to bubbles generated by breaking waves. Here, the 30-min time series were discarded if more than 30% of the data from one ADV, or more than 25% of the data from both ADVs were below the threshold. A total of 458 out of 912 30-min time series (~50%) passed these two tests. For the retained time series, consecutive data points with low signal or correlation spanning less than 1 s are linearly interpolated (Elgar et al. 2001; Feddersen 2010). Long (>1 s) periods with bad data from both ADVs are replaced with a constant value equal to the average over the data points. The number of data points in retained 30-min data runs with low signal amplitude increases with decreasing water levels at the upper sensor because the sensor is closer to the surface. The fraction of data with low amplitudes at the lower sensor and with low correlations at either sensor is not correlated with mean water level.

Velocity time series are despiked using a phase-space method (Mori et al. 2007; Feddersen 2010; Ruessink 2010). A 3D Poincare map is drawn with the velocity and its first and second time derivatives. Data points that fall outside the ellipsoid formed in the Poincare map are replaced with interpolated values.

The turbulent velocity fluctuations u_i' are obtained by removing the wave orbital velocities from the quality-controlled and demeaned velocity time series $u_i - \overline{u}_i$ through an adaptive-filtering technique (Shaw and Trowbridge 2001; Feddersen and Williams 2007):

$$u_{1i}'(t) = [u_{1i}(t) - \overline{u}_{1i}] - \sum_{j=-(N-1)/2}^{(N-1)/2} h_t(j)[u_{2i}(t + j\Delta t) - \overline{u}_{2i}]\Delta t, \tag{9}$$

where subscripts 1 or 2 indicate the bottom or top sensor, i represents the velocity component (cross-shore u, alongshore v, or vertical w), N is the number of filter weights h_t obtained using least squares (Shaw and Trowbridge 2001), $\overline{u}$ is the time-averaged mean velocity, and Δt is the time between adjacent samples. Here, $N = 145$ (Shaw and Trowbridge 2001) resulting in a 9-s filtering window, which is comparable to the mean wave period.

Long (>1 s) periods with bad data from a single ADV are then eliminated in both turbulence fluctuation time series to avoid contamination of the turbulence signal (Feddersen 2010). This "patching" of time series decreases the low-frequency turbulence spectra and may change the frequency distribution of energy (Feddersen 2010), but comparisons of spectra for "patched" and "unpatched" time series show the effects are small because only a few large data gaps exist.

Turbulence auto- and cross-spectra were computed for all data by splitting the data into four subsections with 75% overlap using a Hanning window to suppress sidelobes and merging eight adjacent frequency bands, providing 64 degrees of freedom. Time periods with autospectra not exhibiting an inertial subrange (−5/3 slope) or cross-spectra not exhibiting a −7/3 slope (Biferale and Procaccia 2005; Rosman and Gerbi 2017) were excluded from further analysis, resulting in retaining 116 half-hour periods (~25%). The noise floor of the autospectra (used for normal stresses) is estimated from the flat high-frequency region between 3 and 8 Hz for u' and v', and between 6 and 8 Hz for w'. The noise floor of the cross-spectra (used for shear stresses) is estimated between 3 and 8 Hz. Reynolds normal ($\overline{u_i'^2}$) and shear stresses ($\overline{u_i'u_j'}$) are calculated by integrating the power spectra of the turbulence velocities over the full frequency range minus the noise floor.

3. Results

a. 2D anisotropy

Estimated c_t usually is larger than 1 (Fig. 3). The estimated c_t is smaller for the top ADV (Fig. 3, blue symbols) than for the bottom ADV (Fig. 3, red symbols) indicating that the ratio of cross-shore to vertical turbulence fluctuations increases toward the bed (Scott et al. 2005; Yoon and Cox 2010). Additionally, c_t increases weakly with the ratio (r_F) of local to offshore (4.5-m mean depth) sea-swell energy flux (Fig. 3a, NOAA 2024), defined as

$$r_F = \frac{\frac{1}{16}H_s^2 c_{g,\mathrm{ADV}}}{\int_{f=0.06\mathrm{Hz}}^{f=0.50\mathrm{Hz}} E_{w,4.5\,\mathrm{m}}(f)c_{g,4.5\mathrm{m}}(f)df}, \tag{10}$$

where $E_{w,4.5\mathrm{m}}$ and $c_{g,4.5\mathrm{m}}$ are the wave spectra and group velocity in 4.5-m mean water depth and $c_{g,\mathrm{ADV}}$ is the group velocity at the sensor location, suggesting that the 2D anisotropy may increase toward the outer surfzone consistent with prior studies (Yoon and Cox 2010). Estimated c_t decreases gradually with increasing vertical shear of the mean cross-shore current, defined as the absolute value of the difference of the mean cross-shore velocity measured by the two ADVs, $|\Delta u|$, divided by the distance between the sample volumes (Δz, Fig. 3b), similar to prior studies of anisotropy of homogeneous shear flow (Pope 2000). The 2D anisotropy at the upper sensor decreases

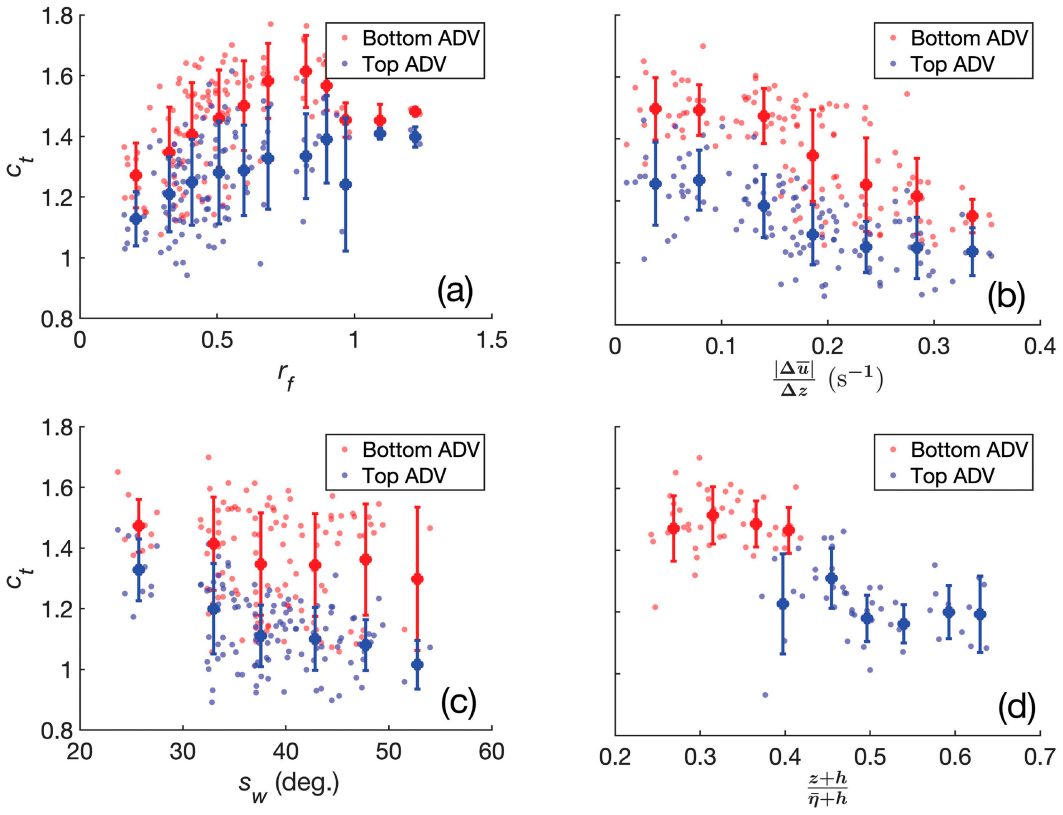

FIG. 3. Two-dimensional anisotropy parameter c_t estimated at the bottom (red) and top (blue) ADVs vs (a) the ratio r_F of the local to 4.5-m-depth energy flux, (b) vertical shear of the cross-shore current $|\Delta u|/\Delta(z)$, (c) wave directional spread s_w, and (d) sensor location above the seafloor $z + h$ relative to the total mean water depth for cases with weak vertical shear of the cross-shore current ($|\Delta u|/\Delta z < 0.16$ s^{-1}). Small dots are 30-min estimates, and larger solid circles and vertical bars are means and standard deviations over bins of 0.1 in (a), 0.05 s^{-1} in (b), 5.7° in (c), and 0.05 in (d). Squared correlations [95% confidence intervals] between 30-min-estimated c_t and (a) the energy flux ratio are 0.25 [0.12, 0.39] and 0.20 [0.08, 0.34] for the top and bottom ADVs, (b) the vertical shear of the cross-shore mean flow is 0.39 [0.25, 0.53] and 0.45 [0.31, 0.58] for the top and bottom ADVs, (c) the directional spread is 0.22 [0.10, 0.36] for the top ADV and roughly 0 for the bottom ADV, and (d) the normalized sensor location is 0.49 [0.23, 0.63] for combined data from both ADVs.

with increasing directional spread s_w (Fig. 3c), possibly because the alongshore component of wave motion stretches the turbulence in the alongshore direction and enhances alongshore normal stresses, making them more "rounded." Wave directional spread has a greater effect on c_t at the upper than the lower sensor, consistent with breaking waves affecting near-surface but not near-bed turbulence. The 2D anisotropy is smaller at the sensor that is higher in the water column, indicating that proximity to the seafloor may confine the vertical structure of turbulence (Fig. 3d).

Anisotropy for low frequencies (c_t calculated with Reynolds stresses filtered for $f < 0.05$ Hz) is larger than that estimated over the region of the turbulence velocity spectra with a $-5/3$ slope (the identifiable inertial subrange), which typically is between 1.0 and 1.6 Hz, well above the wave peak, at both ADVs (Fig. 4a), consistent with prior results showing that turbulent anisotropy increases with decreasing frequency and wavenumber in coastal regions (Thomson et al. 2012). At low frequencies, anisotropy is somewhat smaller at the top than at the bottom ADV (Fig. 4b, red dots), whereas inertial subrange anisotropy is similar at both locations (Fig. 4b, blue dots), indicating that turbulence is confined more by the distance to the seafloor at low frequencies.

At low frequencies, 2D anisotropy is correlated weakly with the vertical shear of the mean cross-shore current (Fig. 5), similar to the total c_t (Fig. 3b). However, the anisotropy is larger at low frequencies and approaches the anisotropy for boundary layer turbulence when the vertical shear is large (Fig. 5, black dashed line; Svendsen 1987). Over the inertial subrange, 2D anisotropy is uncorrelated with bulk wave or current properties (not shown), suggesting that the high-frequency turbulence is independent of background flows.

b. 3D anisotropy

The parameter r_k [Eq. (5)] describes the importance of alongshore relative to cross-shore and vertical normal stresses (Stive and Wind 1982; Svendsen 1987; Larsen and Fuhrman 2018). Estimated r_k at both ADVs are similar (Fig. 6a,

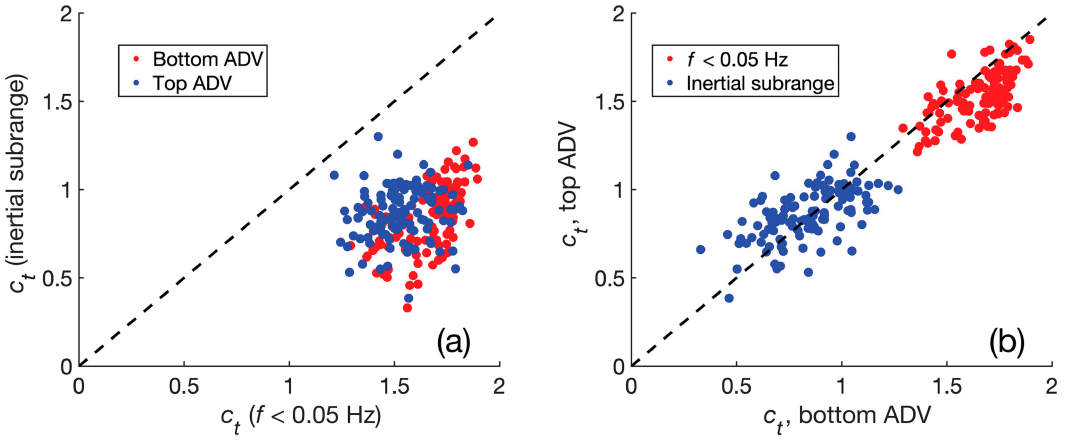

FIG. 4. (a) Inertial subrange 2D anisotropy c_t vs low-frequency ($f < 0.05$ Hz) 2D anisotropy c_t for the bottom (red) and top ADVs (blue), and (b) 2D anisotropy c_t for the top ADV vs c_t for the bottom ADV for low-frequency ($f < 0.05$ Hz, red) and for the inertial subrange (blue).

compare blue dots with red dots) and increase with alongshore current speed, indicating that alongshore normal stresses are owing primarily either to alongshore current vertical shear or to leaking of wave momentum in the alongshore direction. Values are near those for a plane wake (1.33; Svendsen 1987) when the alongshore current is negligible and increase to those for the outer bottom boundary layer (1.8; Svendsen 1987) as the current speed approaches 0.8 m s^{-1} (suggesting that the flow-driven bottom boundary layer may reach the top ADV). The r_k estimated here is similar to that estimated in a prior field study (Ruessink 2010; $r_k = 1.6$) for alongshore flow speeds of about 0.4 m s^{-1}. The ratio of alongshore to cross-shore normal stresses increases weakly with increasing wave directional spread (Fig. 6b), independent of mean alongshore speed (not shown).

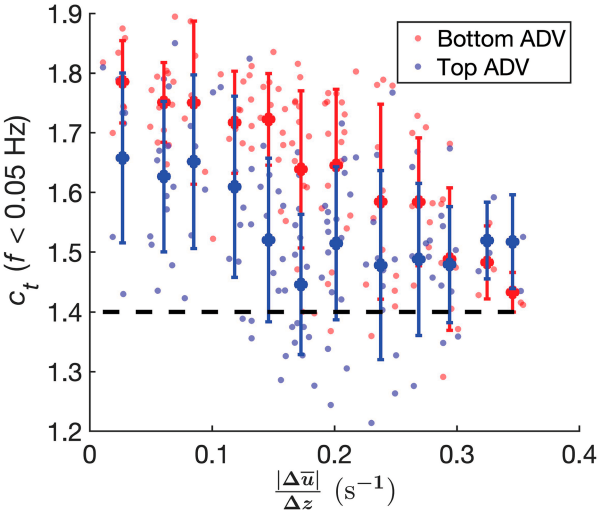

FIG. 5. Low-frequency ($f < 0.05$ Hz) 2D anisotropy c_t vs estimated vertical shear of the cross-shore current at the bottom (red) and top ADVs (blue). Small dots are estimates for 30-min time series, and larger solid circles and vertical bars are means and standard deviations over bins of 0.03 s^{-1}. The horizontal black dashed line is the anisotropy for boundary layer turbulence (Svendsen 1987). Squared correlations [95% confidence intervals] between 30-min-estimated c_t and vertical velocity shear are top ADV $r^2 = 0.14$ [0.04, 0.26] and bottom ADV $r^2 = 0.40$ [0.27, 0.53].

A barycentric map provides an aid to visualize the anisotropy tensor b_{ij} (Lumley 1978) independent of the choice of coordinate system (Pope 2000; Banerjee et al. 2007). Reordering the tensor with the eigenvalues on the diagonalized $\hat{b}_{ij}$ allows identification (appendix A) of three limiting states that are connected by lines in an equilateral triangle: 1-component (only one component of turbulent kinetic energy is nonzero), 2-component (turbulence is isotropic within a plane and is zero in the third dimension), and isotropic. Each anisotropy tensor b_{ij} is then represented by a point in the triangle, whose coordinate is the linear combination of the coordinates of the vertices that represent the above three limiting states (appendix A). The distance from a point in the triangle to each of the three vertices represents the difference between the turbulent state and the limiting states. Measurements from both ADVs are anisotropic (Figs. 7a,b, all data points are far from the top vertex, which represents isotropy). The coefficient C_3 of the isotropic state (see appendix A) is smaller for the bottom ADV (red dots in Fig. 7c) than the top ADV (blue dots in Fig. 7c), especially for weak current vertical shear, indicating that turbulent anisotropy is higher closer to the bed, owing primarily from reduced vertical turbulence near the seafloor. Anisotropy decreases for increasing total vertical current shear (Fig. 7c, the isotropic coefficient C_3 increases) and becomes more rounded in the horizontal direction rather than favoring a single cross-shore direction ["yellower" points are closer to the top vertex and to the axisymmetric contraction line between isotropic and 2-component turbulence (Figs. 7a,b), with a larger coefficient for 2-component states, Fig. 7d]. Anisotropy is smaller (points are closer to the isotropy vertex) for the inertial subrange frequencies than for all frequencies (cf. Figs. 8a,b with Figs. 7a,b) or for the low-frequency range (cf. Figs. 8a,b with Figs. 8c,d). Inertial

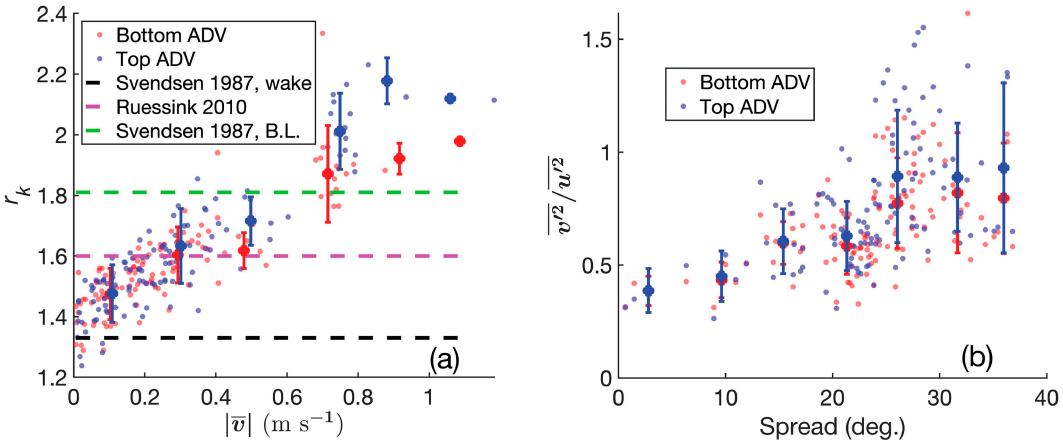

FIG. 6. (a) The r_k estimated at the bottom (red) and top ADVs (blue) vs alongshore current speed $|\overline{v}|$. Small dots are estimates for 30-min time series, and larger solid circles and vertical bars are means and standard deviations over bins of 0.2 m s^{-1}. The horizontal black, magenta, and green dashed lines are estimated r_k for a plane wake (Svendsen 1987), surf-zone observations (Ruessink 2010), and an outer bottom boundary layer (Svendsen 1987). Squared correlations [95% confidence intervals] between 30-min-estimated r_k and $|\overline{v}|$ are top ADV $r^2 = 0.81$ [0.73, 0.86] and bottom ADV $r^2 = 0.72$ [0.62, 0.80]. (b) Ratio of alongshore to cross-shore normal stresses vs wave directional spread (excluding reflected waves) at the bottom (red) and top ADVs (blue). Small dots are estimates for 30-min time series, and larger solid circles and vertical bars are means and standard deviations over bins of 5.7 s. Squared correlations [95% confidence intervals] between 30-min-estimated stress ratios and spreads are top ADV $r^2 = 0.25$ [0.12, 0.39] and bottom ADV $r^2 = 0.24$ [0.12, 0.38].

subrange anisotropy is independent of external wave or current properties, such as vertical current shear. For the low-frequency range, the turbulence at the bottom ADV is more anisotropic than that at the top ADV, similar to the 2D anisotropy estimates (Fig. 4b) and the total Reynolds stress tensor (Fig. 7c). The anisotropy approaches the 2-component limit (bottom-left vertex) with increasing mean-flow vertical shear (Fig. 8f).

The dominant principal component (the eigenvector associated with the largest eigenvalue of the anisotropic tensor transformation matrix) roughly is horizontal at low frequencies, with the vertical direction being least dominant. The angle of the principal axis is between 27° and 57° north of offshore for $-90° <$ angle range $< 90°$ assuming symmetry. The principal axis of low-frequency turbulence (referred to as the turbulence angle below) is similar for both ADVs (not shown). The turbulence angle typically is between the flow direction [$\theta_c = \arctan(\overline{v}/\overline{u})$, blue dots in Fig. 9 fall below the 1:1 line] and the mean wave direction (θ_w, red dots in Fig. 9). A weighted current and wave angle θ_{c+w} is calculated as

$$\theta_{c+w} = \theta_c\sqrt{\overline{u}^2 + \overline{v}^2} + \theta_w\sqrt{\sigma_u^2 + \sigma_v^2}, \tag{11}$$

where σ_u and σ_v are the root-mean-square (rms) cross- and alongshore orbital velocities, respectively. The turbulence angle is aligned and correlated more closely with the weighted angle (orange dots in Fig. 9), indicating that turbulent anisotropy likely is related to the combined current and wave.

4. Discussion

a. *Effect of sensor separation on turbulent anisotropy*

The sensor separation is assumed to be smaller than the wave scale and larger than the turbulent length scale to ensure the wave signal is correlated and turbulence is uncorrelated between the two sensors (Shaw and Trowbridge 2001; Feddersen and Williams 2007). The separation of the vertically stacked sensors was constrained by the need to avoid the surface and bubbles (Elgar et al. 2005) and the sediment and bottom boundary layer. The sensor separation here is about 0.7–1.3 of the turbulence length scale estimated in prior studies (Feddersen 2012), suggesting that some turbulence may be correlated between the two sensors, and thus missed from the estimate of turbulence energy, especially in the low-frequency range (large length scales). However, the quantitative effect of sensor separation on turbulent anisotropy is uncertain.

The effect of the sensor separation on the anisotropy estimates is evaluated assuming that turbulence is advected by both the current and waves (Rosman and Gerbi 2017; Trowbridge et al. 2018; see appendix B). A theoretical test of the effect of sensor separation on the 2D anisotropy is conducted by assuming the wavenumber spectra $\Phi_{ij}(\boldsymbol{\kappa})$ has the form (Lumley and Terray 1983; Rosman and Gerbi 2017):

$$\begin{aligned}
\Phi_{ij}(\boldsymbol{\kappa}) &= \frac{E(|\boldsymbol{\kappa}|)}{4\pi|\boldsymbol{\kappa}|^2}\left(\delta_{ij} - \frac{\kappa_i\kappa_j}{|\boldsymbol{\kappa}|^2}\right)\\
E(|\boldsymbol{\kappa}|) &= C\epsilon^{2/3}|\boldsymbol{\kappa}|^{-5/3}f_L(|\boldsymbol{\kappa}|L)f_\eta(|\boldsymbol{\kappa}|L_\eta)\\
f_L(|\boldsymbol{\kappa}|L) &= \left\{\frac{|\boldsymbol{\kappa}|L}{[(|\boldsymbol{\kappa}|L)^2 + 4\pi^2]^{1/2}}\right\}^{11/3}\\
f_\eta(|\boldsymbol{\kappa}|L_\eta) &= \exp\left(-c_\beta\{[(|\boldsymbol{\kappa}|L_\eta)^4 + c_\eta^4]^{1/4} - c_\eta\}\right),
\end{aligned} \tag{12}$$

where $E(|\boldsymbol{\kappa}|)$ is the energy spectrum, $\boldsymbol{\kappa}$ is the 3D wavenumber vector, κ_i is the ith component of $\boldsymbol{\kappa}$, ϵ is the dissipation rate, L is the rolloff length scale, and L_η is the Kolmogorov length scale

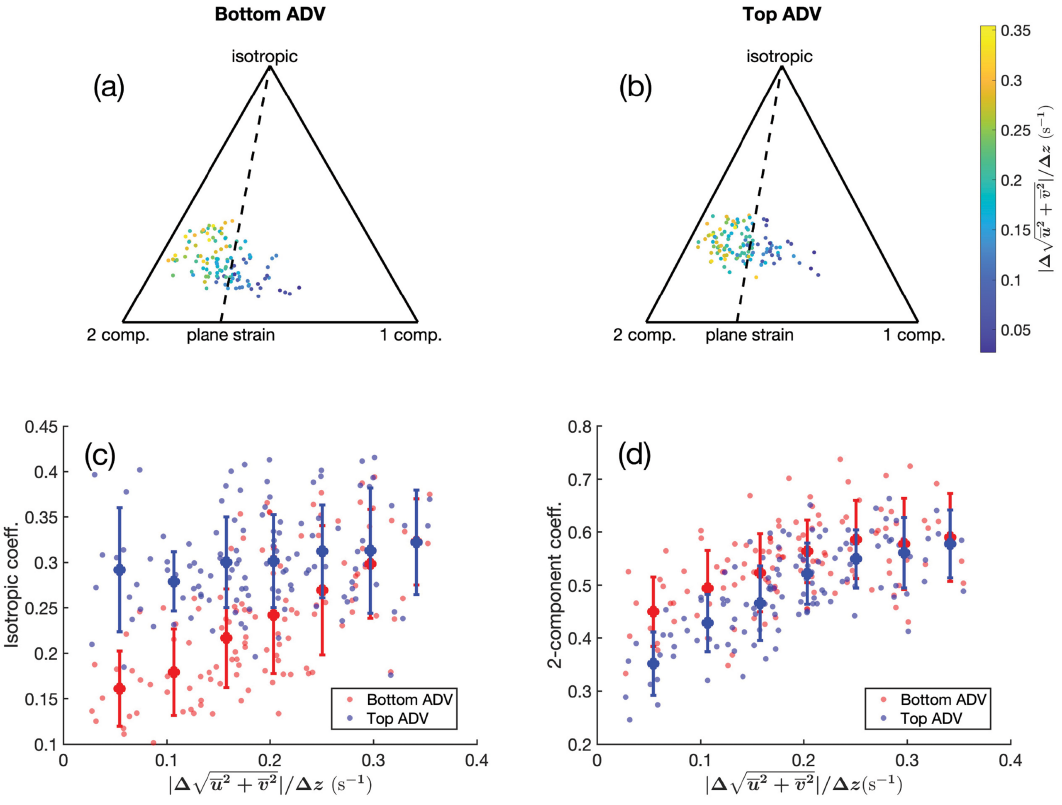

FIG. 7. Barycentric maps of the turbulent anisotropic tensor [the limiting states of isotropic, 2-component (planar), or 1-component (line) are at the top, bottom left, and bottom right vertices] for data from the (a) bottom and (b) top ADVs, colored by the total vertical shear (color bar on right). The dashed lines are the anisotropy for plane strain turbulence (Banerjee et al. 2007; McCaffrey et al. 2015). Coefficients (small colored circles) for the (c) isotropic (C_3) and (d) 2-component states (C_2) for the bottom (red) and top (blue) ADVs vs current vertical shear. The large solid dots and vertical bars are means and standard deviations over bins of 0.05 s^{-1}.

defined as $L_\eta = (\nu^3/\epsilon)^{1/4}$, where ν is the kinematic viscosity (Rosman and Gerbi 2017). The free parameters are estimated as $C = 1.5$, $c_\beta = 5.2$, and $c_\eta = 0.4$ (Pope 2000). The rolloff length scale is set to be $L = 0.3$ m, and the dissipation rate is set to be 10^{-3} m^2 s^{-3}.

For a relatively small cross-shore current of 0.15 m s^{-1} (Fig. 2b) with negligible wave advection (relative to the current advection), but retaining wave filtering, the low-frequency energy decreases with decreasing vertical sensor separation Δz (normalized by the rolloff length scale L) in both the cross-shore and vertical directions (Fig. 10). For a normalized distance ($\Delta z/L$) of 0.5, the low-frequency turbulence energy density is nearly twice the original levels in the cross-shore direction and is similar to the original levels in the vertical direction. The "anisotropy" owing to sensor separation is about 0.2 for $\Delta z/L$ larger than 0.5 (Fig. 10c), which is small compared with the observed anisotropy (Figs. 3–5). The energy levels are not affected by the separation distance at frequencies higher than those associated with the rolloff length scale L ($f/f_0 > 1$ on Figs. 10a,b), and thus anisotropy owing to sensor separation is near 0 at these frequencies.

b. *Turbulent length scale anisotropy*

Wave advection in energetic conditions can distort the frequency spectrum, decreasing energy at low frequencies and increasing energy at high frequencies (Lumley and Terray 1983; Rosman and Gerbi 2017), and the transformation from frequency to wavenumber spectra often is underdetermined. Assuming the theoretical form of the wavenumber spectrum above [Eq. (12)], the wavenumber spectrum at low wavenumber scales as (Rosman and Gerbi 2017)

$$\Phi_{ij,\mathrm{low}}(\boldsymbol{\kappa}) \propto \epsilon^{2/3} L^{5/3}, \tag{13}$$

and at high wavenumber scales as

$$\Phi_{ij,\mathrm{high}}(\boldsymbol{\kappa}) \propto \epsilon^{2/3}. \tag{14}$$

Estimating the dissipation rate from the inertial range of the vertical velocity spectrum (Feddersen et al. 2007), the turbulent length scale is calculated by mapping the wavenumber spectrum to the frequency spectrum. Scaling the estimated (from observations) and theoretical frequency spectra by $\epsilon^{-2/3}$, the turbulent length scale is then calculated as

$$L_{\mathrm{data}} = \left\{ \left[\frac{S_{u_i' u_j',\mathrm{low}}(f)}{S_{\mathrm{model,low}}(f)} \right] L_{\mathrm{model}}^{5/3} \right\}^{3/5}, \tag{15}$$

where $S_{u_i' u_j',\mathrm{low}}(f)$ and $S_{\mathrm{model,low}}(f)$ are the low-frequency parts of the estimated and theoretical turbulent velocity frequency

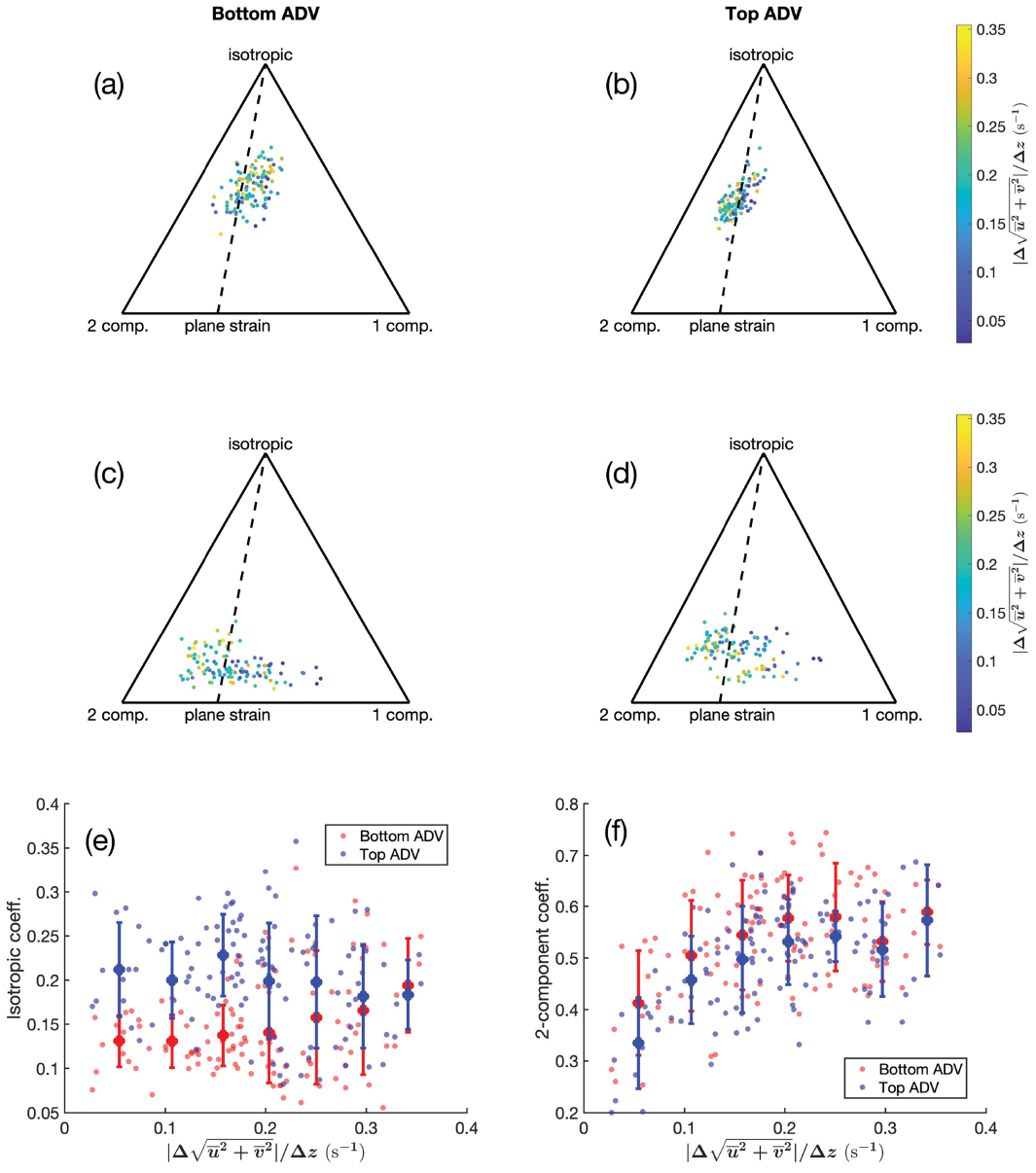

FIG. 8. Barycentric maps of the turbulent anisotropic tensor [the limiting states of isotropic, 2-component (planar), or 1-component (line) are at the top, bottom left, and bottom right vertices] for data from the (a),(c) bottom and (b),(d) top ADVs for (a),(b) the inertial subrange and (c),(d) $f < 0.05$ Hz, colored by the total vertical shear (color bar on right). The dashed lines are the anisotropy for plane strain turbulence (Banerjee et al. 2007; McCaffrey et al. 2015). The coefficients (small colored circles) for the (e) isotropic and (f) 2-component states for the bottom (red) and top (blue) ADVs for $f < 0.05$ Hz vs current vertical shear. The large solid dots and vertical bars are means and standard deviations over bins of 0.05 s^{-1}.

spectra, respectively, and L_{model} is the rolloff length scale of the theoretical wavenumber spectrum [Eq. (12)].

Normalized (by water depth) cross- and alongshore turbulent length scales are similar (Fig. 11, compare blue with orange curves) and are larger than the vertical length scale (yellow curve). The ranges of normalized horizontal (0.5–1.5) and vertical (0.2–0.5) length scales are similar to previous estimates [0.5–0.8 and 0.1–0.2 for horizontal and vertical scales, respectively (Trowbridge and Elgar 2003; Feddersen and Williams 2007)]. Length scales calculated from both sensors typically are similar (not shown). Although advected by both waves and currents, the ratios of horizontal to vertical length scale are weakly correlated with the ratios of horizontal to vertical low-frequency ($f < 0.05$ Hz) spectral energy (not shown), similar to 3D anisotropy (Figs. 7 and 8).

c. *Wave bias*

Although adaptive filtering removes the wave signal reasonably well (Feddersen and Williams 2007), a residual wave bias may remain in the normal stresses, especially near the

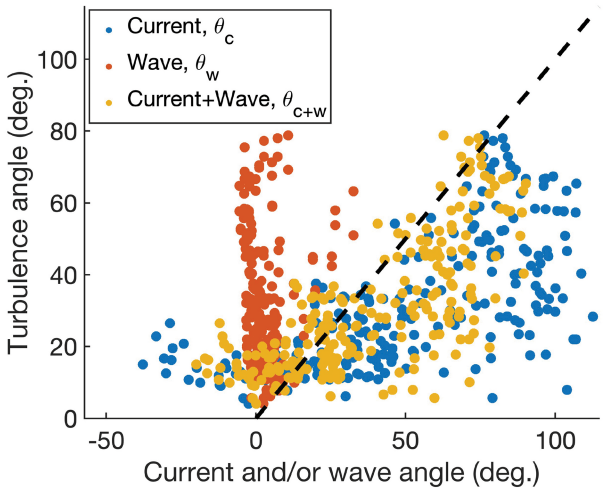

FIG. 9. Turbulence angle relative to the cross-shore direction of low-frequency turbulence vs angle of the current θ_c (blue), wave θ_w (red), and energy-weighted current and wave θ_{c+w} (orange) for both ADVs. The squared correlations [95% confidence intervals] of the turbulence angle at the top and bottom ADVs with the current, wave, and energy-weighted angles are $r^2 = 0.34$ [0.24, 0.44], $r^2 = 0$, and $r^2 = 0.53$ [0.44, 0.62], respectively.

peak frequency (appendix C). The wave bias can be estimated from the first terms in Eq. (C6), which are roughly an order of magnitude larger than the second terms. Specifically, estimating $\sigma^2_{u'}$, which is the rms of the cross-shore turbulence velocity fluctuations, as $O(10^{-2})$ m^2 s^{-2} (Ruessink 2010), σ^2_u as $O(10^{-1})$ m^2 s^{-2}, and assuming $\theta_{\text{tilt}} = 0.05$, $\delta_u = 0.5$, $\delta_w = 0.2$, $\Delta z/z = 0.5$, and $\kappa_w z = 0.3$ (Feddersen and Williams 2007), the ratio $r_{u'}$ of the cross-shore wave bias to the turbulence signal is

$$r_{u'} \approx \frac{\delta_u^2\left(\frac{\Delta z}{z}\right)^2(\kappa_w z)^4\sigma_u^2}{\sigma^2_{u'}} \approx \frac{5\times10^{-4}\sigma_u^2}{\sigma^2_{u'}}, \tag{16}$$

which is $O(10^{-2})$, suggesting that it is unlikely that $\overline{u'^2}$ is dominated by wave bias. The ratio $r_{w'}$ of the vertical wave bias to turbulence is

$$r_{w'} \approx \frac{\delta_w^2\left(\frac{\Delta z}{z}\right)^2\sigma_w^2}{\sigma^2_{w'}} \approx \frac{0.01\sigma_w^2}{\sigma^2_{w'}}, \tag{17}$$

with σ^2_w estimated as $O(10^{-2})$ m^2 s^{-2} based on observations and $\sigma^2_{w'}$ is $O(10^{-3})$ m^2 s^{-2} based on observations and previous studies (Ruessink 2010). Although the wave bias may be more significant in the vertical than the horizontal normal stresses, it is unlikely to dominate the estimates.

d. Limitations

Physical understanding of turbulence energy transfers and dissipation in the surfzone is limited, at least partly owing to issues obtaining measurements under breaking waves. In particular, estimates of phase-resolved turbulence (George et al. 1994) are rare. As in prior studies (Feddersen and Williams 2007; Ruessink 2010), here the investigation of anisotropy focuses on wave averaged properties. Turbulence injection from breaking waves is phase-dependent, especially in plunging conditions (Ting and Kirby 1995; Na et al. 2016, 2020), which may induce a nonlinear response from the ensemble flow, such as shearing near the interface (Na et al. 2016, 2020) and asymmetrical turbulence straining (Teixeira and Belcher 2002). The resulting phase-dependent turbulent anisotropy and ensemble strained flow may produce a phase-dependent energy cascade that cannot be resolved in a phase-averaged analysis. Higher-frequency and more accurate turbulence measurements with simultaneous ensemble flow shear observations would elucidate the physical mechanisms that affect surfzone turbulence anisotropy.

Many physical properties of natural surfzones, including wave directional spread, vertical shear of the cross-shore current, and the location within the surfzone (e.g., variables on the x axis of Fig. 3) may be correlated with each other, making it difficult to determine which processes are affecting the anisotropy. Although variables studied here are correlated significantly with c_t in a multiple regression, controlled experiments are needed to determine the causal relationships of wave and current properties with turbulence anisotropy.

Wave–turbulence decoupling also remains a challenging topic. The two-sensor method used here partially neglects the signal contained in length scales larger than the sensor separation (section 4a). One-sensor methods have been developed that do not require vertically stacked or synchronized sensors to measure turbulence (Benilov and Filyushkin 1970; Bricker and Monismith 2007). Two-dimensional anisotropy (c_t) estimated over all frequencies with the phase method (Bricker and Monismith 2007) is slightly larger than that estimated here with the two-sensor method (Fig. 3), but it has similar dependence on wave and flow properties (not shown). Reynolds stresses using the phase method also are larger than those here (not shown). The phase method interpolates the velocity spectrum below the wave peak (which is assumed to be turbulence), whereas the two-sensor method used here removes the coherent low-frequency signal (which is assumed to be owing to waves) (Bricker and Monismith 2007; Feddersen and Williams 2007). Therefore, turbulence spectral levels are similar over the inertial subrange but are higher at low frequencies for the phase method than for the two-sensor method.

Other single-sensor methods, including the ensemble empirical mode decomposition (EEMD; Huang and Wu 2008), synchronized wavelet transform (SWT; Bian et al. 2018), and dynamical mode decomposition (DMD; Chávez-Dorado et al. 2024), have been developed recently. In the laboratory, both EEMD and SWT underpredict turbulence intensity in the wave dominated frequency range for wind-driven irregular

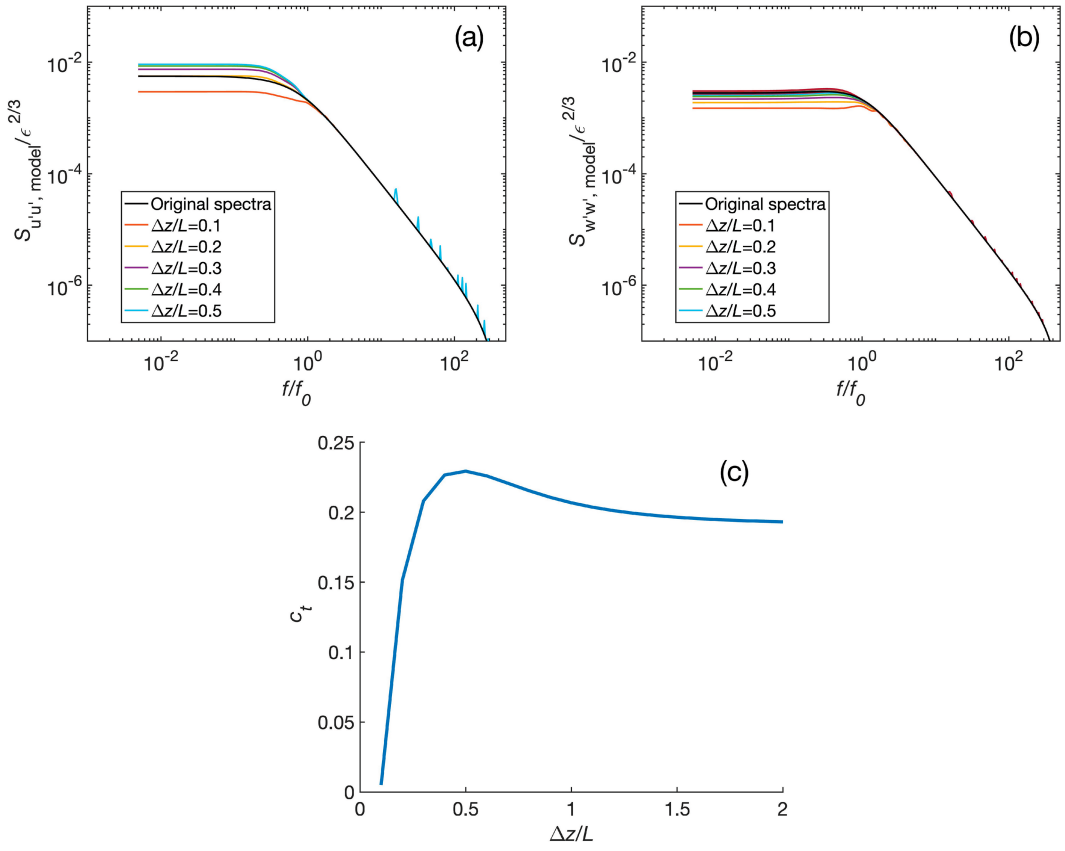

FIG. 10. (a) Cross-shore and (b) vertical turbulence energy density scaled by dissipation rate vs frequency normalized by that associated with the rolloff length scale [$f_0 = (0.15\ \mathrm{m\ s^{-1}})/2\pi L$] for normalized sensor separation distances of 0.1 (red), 0.2 (yellow), 0.3 (purple), 0.4 (green), and 0.5 (light blue). (c) Anisotropy parameter c_t vs sensor separation normalized by rolloff length scale.

waves with intermittent breaking (Chávez-Dorado et al. 2024). Although the DMD method performs reasonably well, the turbulence estimates are sensitive to the free parameters that are determined case by case (Chávez-Dorado et al. 2024). Thus, although a more accurate method to estimate turbulence would lead to new knowledge, the two-sensor filtering techniques used here remain a good choice for surfzone studies.

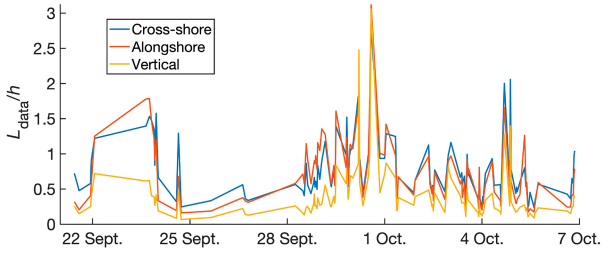

FIG. 11. Cross-shore (blue curve, mean = 0.76, median = 0.62, standard deviation = 0.44 L_{data}/h), alongshore (orange curve, mean = 0.72, median = 0.60, standard deviation = 0.47 L_{data}/h), and vertical (yellow curve, mean = 0.39, median = 0.27, standard deviation = 0.40 L_{data}/h) vs time (day month in 2023).

5. Conclusions

Turbulent anisotropy under breaking waves is investigated using surfzone observations from two vertically stacked velocimeters in about 2-m water depth. In contrast to common model parameterizations for turbulence, the cross-shore vertical (2D) turbulent anisotropy parameter c_t is larger than 1 and is dependent on frequency, proximity to the bed, the ratio of local to offshore wave energy flux, and vertical shear of the cross-shore current. Waves may have a greater influence on anisotropy near the water surface. Low-frequency anisotropy decreases with increasing vertical shear of the cross-shore current.

Alongshore normal stresses increase with increasing alongshore flow, with their ratio to cross-shore and vertical normal stresses roughly consistent with the classical wake approximation for weak currents, and increase to that expected for an outer bottom boundary layer during strong currents. Turbulence becomes less anisotropic and more similar to axisymmetric contraction as vertical shear increases. Relative to inertial subrange turbulence, low-frequency turbulence is more similar to the two-component limit. The principal axis of the turbulence anisotropy tensor is correlated with a weighted wave–current angle, indicating that 3D turbulence is affected by

both waves and mean currents. The vertical turbulent length scales are estimated to be a fraction of the water depth, and the horizontal length scales are roughly equal to the water depth, similar to prior studies.

Acknowledgments. We thank the staff at the Field Research Facility and the PVLAB field crew for deploying, maintaining, and recovering sensors in often difficult surfzone conditions, Dr. Malcolm Scully for input regarding the stack configuration and time-sync technique, Dr. John Trowbridge and Professor Johanna Rosman for invaluable insights on wave and current advection on turbulence, and Professor Glenn Flierl for useful discussions on anisotropic turbulence structures. We thank Dr. Falk Feddersen and the anonymous reviewers for providing constructive feedback. Funding was provided by the National Science Foundation, the WHOI Ocean Venture Fund, a MathWorks Fellowship, and a Vannevar Bush Faculty Fellowship.

Data availability statement. Field data are available online at https://doi.org/10.5281/zenodo.13737274 (Chen et al. 2024a). Bathymetry surveys and incident wave conditions (17- and 4.5-m water depth) are available at https://chlthredds.erdc.dren.mil/thredds/catalog/frf/catalog.html (USACE 2024). NOAA water levels are at https://tidesandcurrents.noaa.gov/stationhome.html?id=8651370 (NOAA 2024).

APPENDIX A

Mapping of Anisotropy Tensor b_{ij}

For each anisotropy tensor b_{ij}, its diagonalized matrix $\hat{b_{ij}}$ can be found as a set of linear combinations of the three limiting states ($\hat{\mathbf{a}}_1$, $\hat{\mathbf{a}}_2$, $\hat{\mathbf{a}}_3$) as (Banerjee et al. 2007)

$$\hat{b}_{ij} = C_1\hat{\mathbf{a}}_1 + C_2\hat{\mathbf{a}}_2, \tag{A1}$$

$$\hat{\mathbf{a}}_1 = \begin{bmatrix} \frac{2}{3} & 0 & 0 \\ 0 & -\frac{1}{3} & 0 \\ 0 & 0 & -\frac{1}{3} \end{bmatrix} \hat{\mathbf{a}}_2 = \begin{bmatrix} \frac{1}{6} & 0 & 0 \\ 0 & \frac{1}{6} & 0 \\ 0 & 0 & -\frac{1}{3} \end{bmatrix}, \tag{A2}$$

where $\hat{\mathbf{a}}_1$ and $\hat{\mathbf{a}}_2$ represent the 1-component and 2-component states and C_1 and C_2 represent the coefficients for these limiting states, respectively. The isotropic state is represented by a zero matrix $\hat{\mathbf{a}}_3$ and therefore is not included in Eqs. (A1) or (A2). The coefficients are calculated from the eigenvalues λ of b_{ij} as (Banerjee et al. 2007)

$$\begin{aligned} C_1 &= \lambda_1 - \lambda_2 \\ C_2 &= 2(\lambda_2 - \lambda_3) \\ C_3 &= 1 - C_1 - C_2 = 3\lambda_3 + 1, \end{aligned} \tag{A3}$$

where $\lambda_1 \geq \lambda_2 \geq \lambda_3$ and C_3 represents the coefficient for the isotropic state. The Euclidean coordinates (x_b, y_b) of b_{ij} on a barycentric map are then calculated as the linear combination of the coordinates (x_1, y_1), (x_2, y_2), and (x_3, y_3) of the three limiting states ($\hat{\mathbf{a}}_1$, $\hat{\mathbf{a}}_2$, $\hat{\mathbf{a}}_3$; Banerjee et al. 2007):

$$\begin{aligned} x_b &= C_1x_1 + C_2x_2 + C_3x_3 \\ y_b &= C_1y_1 + C_2y_2 + C_3y_3. \end{aligned} \tag{A4}$$

APPENDIX B

Derivation of the Effect of Sensor Separation on Turbulent Anisotropy

The turbulence time series can be written as a Fourier–Stieltjes integral (Trowbridge et al. 2018):

$$u_i'(\mathbf{x}, t) = \int_{\boldsymbol{\kappa}} d\hat{u}_i(\boldsymbol{\kappa}, t)e^{i\boldsymbol{\kappa}\cdot\mathbf{x}}d\boldsymbol{\kappa}, \tag{B1}$$

where $\mathbf{x}$ is the 3D location of the sensor and $d\hat{u}_i$ is the complex Fourier–Stieltjes amplitude. Under the "Taylor frozen turbulence" hypothesis, wave and current advection are included in the exponential as

$$u_i'(\mathbf{x}, t) = \int_{\boldsymbol{\kappa}} d\hat{u}_i(\boldsymbol{\kappa})e^{i\boldsymbol{\kappa}\cdot\mathbf{x}+it\boldsymbol{\kappa}\cdot\bar{\mathbf{u}}+i\boldsymbol{\kappa}\cdot\mathbf{X}(t)}d\boldsymbol{\kappa}, \tag{B2}$$

where $\bar{\mathbf{u}}$ is the 3D mean current and $\mathbf{X}(t)$ is the wave excursion time series.

At a second sensor separated by $\boldsymbol{\Delta}\mathbf{x}$, the corresponding time series is

$$u_i'(\mathbf{x} + \Delta\mathbf{x}, t) = \int_{\boldsymbol{\kappa}} d\hat{u}_i(\boldsymbol{\kappa})e^{i\boldsymbol{\kappa}\cdot\mathbf{x}+i\boldsymbol{\kappa}\cdot\Delta\mathbf{x}+it\boldsymbol{\kappa}\cdot\bar{\mathbf{u}}+i\boldsymbol{\kappa}\cdot\mathbf{X}(t)}d\boldsymbol{\kappa}. \tag{B3}$$

Using the integral form of Eq. (9), turbulence at $(\mathbf{x} + \boldsymbol{\Delta}\mathbf{x}, t)$ that is carried to $(\mathbf{x}, t)$ as

$$\hat{u}_{1i}'(\mathbf{x}, t) = \int_{-T/2}^{T/2} h_t(\tau)\int_{\boldsymbol{\kappa}} d\hat{u}_i(\boldsymbol{\kappa})e^{i\boldsymbol{\kappa}\cdot\mathbf{x}+i\boldsymbol{\kappa}\cdot\Delta\mathbf{x}+i(t-\tau)\boldsymbol{\kappa}\cdot\bar{\mathbf{u}}+i\boldsymbol{\kappa}\cdot\mathbf{X}(t-\tau)}d\boldsymbol{\kappa}d\tau, \tag{B4}$$

where T is the filtered window length and τ is a dummy integration variable. The turbulent fluctuation $\Delta u_i'(\mathbf{x}, t) = u_i'(\mathbf{x}, t) - \hat{u}_{1i}'(\mathbf{x}, t)$ after wave filtering is

$$\begin{aligned} \Delta u_i'(\mathbf{x}, t) &= \int_{\boldsymbol{\kappa}} d\hat{u}_i(\boldsymbol{\kappa})e^{i\boldsymbol{\kappa}\cdot\mathbf{x}+it\boldsymbol{\kappa}\cdot\bar{\mathbf{u}}+i\boldsymbol{\kappa}\cdot\mathbf{X}(t)}d\boldsymbol{\kappa} - \int_{-T/2}^{T/2} h_t(\tau)\int_{\boldsymbol{\kappa}} d\hat{u}_i(\boldsymbol{\kappa})e^{i\boldsymbol{\kappa}\cdot\mathbf{x}} \\ &\quad + i\boldsymbol{\kappa}\cdot\Delta\mathbf{x} + i(t-\tau)\boldsymbol{\kappa}\cdot\bar{\mathbf{u}} + i\boldsymbol{\kappa}\cdot\mathbf{X}(t-\tau)d\boldsymbol{\kappa}d\tau \\ &= \int_{-T/2}^{T/2}\int_{\boldsymbol{\kappa}} d\hat{u}_i(\boldsymbol{\kappa})e^{i\boldsymbol{\kappa}\cdot\mathbf{x}+it\boldsymbol{\kappa}\cdot\bar{\mathbf{u}}}\left[\frac{e^{i\boldsymbol{\kappa}\cdot\mathbf{X}(t)}}{T} - h_t(\tau)e^{i\boldsymbol{\kappa}\cdot\Delta x}\right. \\ &\quad \left. - i\tau\boldsymbol{\kappa}\cdot\bar{\mathbf{u}} + i\boldsymbol{\kappa}\cdot\mathbf{X}(t-\tau)\right]d\boldsymbol{\kappa}d\tau. \end{aligned} \tag{B5}$$

The jth turbulent fluctuation can be calculated similarly at time $t + \sigma$:

$$\begin{aligned} \Delta u_j'(\mathbf{x}, t+\sigma) = \int_{-T/2}^{T/2}\int_{\boldsymbol{\kappa}} d\hat{u}_j(\boldsymbol{\kappa})e^{i\boldsymbol{\kappa}\cdot\mathbf{x}+it\boldsymbol{\kappa}\cdot\bar{\mathbf{u}}+i\sigma\boldsymbol{\kappa}\cdot\bar{\mathbf{u}}}\left[\frac{e^{i\boldsymbol{\kappa}\cdot\mathbf{X}(t+\sigma)}}{T}\right. \\ \left. - h_t(\tau)e^{i\boldsymbol{\kappa}\cdot\Delta x - i\tau\boldsymbol{\kappa}\cdot\bar{\mathbf{u}}+i\boldsymbol{\kappa}\cdot\mathbf{X}(t+\sigma-\tau)}\right]d\boldsymbol{\kappa}d\tau. \end{aligned} \tag{B6}$$

The temporal correlation function $\rho_{\Delta u_i' \Delta u_j'}(\sigma)$ can be calculated by multiplying Eq. (B6) with the complex conjugate of Eq. (B5) and taking the expected values. By using the property that (Trowbridge et al. 2018)

$$\overline{d\hat{u}_{i*}(\boldsymbol{\kappa}')d\hat{u}_j(\boldsymbol{\kappa})} = \Phi_{ij}(\boldsymbol{\kappa})\delta(\boldsymbol{\kappa} - \boldsymbol{\kappa}')d\boldsymbol{\kappa}d\boldsymbol{\kappa}', \tag{B7}$$

and the characteristic function of a Gaussian distribution is given by (Lumley and Terray 1983; Rosman and Gerbi 2017; Trowbridge et al. 2018)

$$\overline{e^{i\boldsymbol{\kappa}[\mathbf{X}(t+t')-\mathbf{X}(t)]}} = e^{-\kappa_m\kappa_n[\overline{X_mX_n} - \overline{X_m(t)X_n(t+t')}]}, \tag{B8}$$

where $\boldsymbol{\kappa}'$ is a dummy wavenumber, t' is a dummy time, X_m is the mth component of wave excursion, and m and n are the Einstein summations; $\rho_{\Delta u_i' \Delta u_j'}(\sigma)$ can be separated into four parts:

$$\begin{aligned}
\rho_{\Delta u_i' \Delta u_j'}(\sigma) = &\int_{\kappa} \Phi_{ij}(\boldsymbol{\kappa}) e^{i\sigma\boldsymbol{\kappa}\cdot\bar{\mathbf{u}}} e^{-\kappa_m\kappa_n[\overline{X_mX_n} - \overline{X_m(t)X_n(t+\sigma)}]} d\boldsymbol{\kappa} \\
&- \int_{-T/2}^{T/2}\int_{\kappa} h_t(\tau)\Phi_{ij}(\boldsymbol{\kappa}) e^{i\sigma\boldsymbol{\kappa}\cdot\bar{\mathbf{u}}} e^{-i\kappa\cdot\Delta x + i\tau\boldsymbol{\kappa}\cdot\bar{\mathbf{u}}} \\
&\times e^{-\kappa_m\kappa_n[\overline{X_mX_n} - \overline{X_m(t)X_n(t+\sigma+\tau)}]} d\boldsymbol{\kappa}d\tau \\
&- \int_{-T/2}^{T/2}\int_{\kappa} h_t(\tau)\Phi_{ij}(\boldsymbol{\kappa}) e^{i\sigma\boldsymbol{\kappa}\cdot\bar{\mathbf{u}}} e^{i\boldsymbol{\kappa}\cdot\Delta x - i\tau\boldsymbol{\kappa}\cdot\bar{\mathbf{u}}} \\
&\times e^{-\kappa_m\kappa_n[\overline{X_mX_n} - \overline{X_m(t)X_n(t+\sigma-\tau)}]} d\boldsymbol{\kappa}d\tau \\
&+ \int_{-T/2}^{T/2}\int_{-T/2}^{T/2}\int_{\kappa} h(\tau_1)h(\tau_2)\Phi_{ij}(\boldsymbol{\kappa}) e^{i\sigma\boldsymbol{\kappa}\cdot\bar{\mathbf{u}}} e^{i(\tau_1-\tau_2)\boldsymbol{\kappa}\cdot\bar{\mathbf{u}}} \\
&\times e^{-\kappa_m\kappa_n[\overline{X_mX_n} - \overline{X_m(t)X_n(t+\sigma+\tau_1-\tau_2)}]} d\boldsymbol{\kappa}d\tau_1 d\tau_2.
\end{aligned} \tag{B9}$$

where τ_1 and τ_2 are the dummy integration variables. The first term of Eq. (B9) is identical to Eq. (7) of Rosman and Gerbi (2017) and Eq. (B12) of Trowbridge et al. (2018) except the separation term, which gives the turbulent correlation function of a given wavenumber spectra Φ_{ij} under current and wave advection. The second and third terms are two cases where the filtering technique affects the turbulence calculation from one sensor. Assuming $h_t(\tau) = h_t(-\tau)$, the second and third terms can be combined as

$$-2\int_{-T/2}^{T/2}\int_{\kappa} h_t(\tau)\Phi_{ij}(\boldsymbol{\kappa})\cos(\boldsymbol{\kappa}\cdot\Delta\mathbf{x}) e^{i\sigma\boldsymbol{\kappa}\cdot\bar{\mathbf{u}}} e^{i\tau\boldsymbol{\kappa}\cdot\bar{\mathbf{u}}} e^{-\kappa_m\kappa_n[\overline{X_mX_n} - \overline{X_m(t)X_n(t+\sigma+\tau)}]} d\boldsymbol{\kappa}d\tau. \tag{B10}$$

Note that the differencing technique proposed by Trowbridge (1998) and used in Trowbridge et al. (2018) is a special case of the filtered weight $h_t(\tau)$, where

$$h_t(\tau) = \delta(0), \tag{B11}$$

where $\delta(0)$ is a Dirac delta function at $\tau = 0$. By using this $h_t(\tau)$, the turbulent correlation function in Eqs. (B9) and (B10) can be simplified to

$$\rho_{\Delta u_i' \Delta u_j'}(\sigma) = \int_{\kappa} \Phi_{ij}(\boldsymbol{\kappa}) e^{i\sigma\boldsymbol{\kappa}\cdot\bar{\mathbf{u}}} e^{-\kappa_m\kappa_n[\overline{X_mX_n} - \overline{X_m(t)X_n(t+\sigma)}]}[2 - 2\cos(\boldsymbol{\kappa}\cdot\Delta\mathbf{x})] d\boldsymbol{\kappa}, \tag{B12}$$

where Eq. (B12) of Trowbridge et al. (2018) is recovered.

The wave advection part in Eqs. (B9), (B10), and (B12) can be simplified as (Trowbridge et al. 2018)

$$\begin{aligned}
&\exp\{-\kappa_m\kappa_n[\overline{X_mX_n} - \overline{X_m(t)X_n(t+\sigma)}]\} \\
&\quad = \exp\left[-\frac{\sigma^2}{2}\kappa_m\kappa_n\int_{-\infty}^{\infty} S_{\tilde{u}_m\tilde{u}_n}(f')\frac{\sin(\sigma f')^2/2}{(\sigma f')^2/2} df'\right],
\end{aligned} \tag{B13}$$

where f' is a dummy frequency variable and $S_{\tilde{u}_m\tilde{u}_n}(f')$ is the spectra of orbital velocities. Using this result in Eqs. (B9) and (B10) gives

$$\begin{aligned}
\rho_{\Delta u_i' \Delta u_j'}(\sigma) = &\int_{\kappa} \Phi_{ij}(\boldsymbol{\kappa}) e^{i\sigma\boldsymbol{\kappa}\cdot\bar{\mathbf{u}}} \\
&\times \exp\left[-\frac{\sigma^2}{2}\kappa_m\kappa_n\int_{\infty}^{\infty} S_{\tilde{u}_m\tilde{u}_n}(f')\frac{\sin(\sigma f')^2/2}{(\sigma f')^2/2} df'\right] d\boldsymbol{\kappa} \\
&- 2\int_{-T/2}^{T/2}\int_{\kappa} h_t(\tau)\Phi_{ij}(\boldsymbol{\kappa})\cos(\boldsymbol{\kappa}\cdot\Delta\mathbf{x}) e^{i\sigma\kappa\cdot\bar{\mathbf{u}}} e^{i\tau\boldsymbol{\kappa}\cdot\bar{\mathbf{u}}} \\
&\times \exp\left\{-\frac{(\sigma+\tau)^2}{2}\kappa_m\kappa_n\int_{-\infty}^{\infty} S_{\tilde{u}_m\tilde{u}_n}(f')\frac{\sin[(\sigma+\tau)f']^2/2}{[(\sigma+\tau)f']^2/2} df'\right\} d\boldsymbol{\kappa}d\tau \\
&+ \int_{-T/2}^{T/2}\int_{-T/2}^{T/2}\int_{\kappa} h(\tau_1)h(\tau_2)\Phi_{ij}(\boldsymbol{\kappa}) e^{i\sigma\boldsymbol{\kappa}\cdot\bar{\mathbf{u}}} e^{i(\tau_1-\tau_2)\boldsymbol{\kappa}\cdot\bar{\mathbf{u}}} \\
&\times \exp\left\{-\frac{(\sigma+\tau_1-\tau_2)^2}{2}\kappa_m\kappa_n\right. \\
&\times \left.\int_{-\infty}^{\infty} S_{\tilde{u}_m\tilde{u}_n}(f')\frac{\sin[(\sigma+\tau_1-\tau_2)f']^2/2}{[(\sigma+\tau_1-\tau_2)f']^2/2} df'\right\} d\boldsymbol{\kappa}d\tau_1 d\tau_2.
\end{aligned} \tag{B14}$$

If wave advection is weak, the exponential terms that include the spectrum approach 1. Therefore, the correlation function [Eq. (B14)] can be simplified as

$$\begin{aligned}
\rho_{\Delta u_i' \Delta u_j'}(\sigma) = &\int_{\kappa} \Phi_{ij}(\boldsymbol{\kappa}) e^{i\sigma\boldsymbol{\kappa}\cdot\bar{\mathbf{u}}}\left\{1 - 2\cos(\boldsymbol{\kappa}\cdot\Delta\mathbf{x})\int_{-T/2}^{T/2} e^{i\tau\boldsymbol{\kappa}\cdot\bar{\mathbf{u}}} h_t(\tau) d\tau\right. \\
&\left. + \left[\int_{-T/2}^{T/2} e^{i\tau\boldsymbol{\kappa}\cdot\bar{\mathbf{u}}} h_t(\tau) d\tau\right]^2\right\} d\boldsymbol{\kappa}.
\end{aligned} \tag{B15}$$

The limits of integration are symmetrical, and the integrand is an even function, and thus the result of integrating τ is real. Defining the integral with weights $h_t(\tau)$ as A, Eq. (B15) gives

$$\rho_{\Delta u_i' \Delta u_j'}(\sigma) = \int_{\kappa} \Phi_{ij}(\boldsymbol{\kappa}) e^{i\sigma\boldsymbol{\kappa}\cdot\bar{\mathbf{u}}}[1 - 2\cos(\boldsymbol{\kappa}\cdot\Delta\mathbf{x})\mathrm{Re}(A) + \mathrm{Re}(A)^2] d\boldsymbol{\kappa}, \tag{B16}$$

where $\mathrm{Re}(A) = \int_{-T/2}^{T/2}\cos(\tau\boldsymbol{\kappa}\cdot\bar{\mathbf{u}})h_t(\tau)d\tau$. The turbulence frequency spectra then can be calculated via Fourier transform. Equation (B16) and its Fourier transform are used with Eq. (12) in section 4a with $\Delta\mathbf{x} = \Delta z$ (sensors are separated vertically) to test the effect of sensor separation on turbulent anisotropy (Fig. 10).

APPENDIX C

Derivation of Wave Bias Estimates

To estimate the wave bias, the demeaned cross-shore and vertical velocities $u_n - \overline{u}_n$ and $w_n - \overline{w}_n$, where n signifies sensor 1 or 2, are defined as (Feddersen and Williams 2007)

$$\begin{aligned} u_n - \overline{u}_n &= \tilde{u}_n + u'_n + \theta_{\text{tilt}}(\tilde{w}_n + w'_n) \\ w_n - \overline{w}_n &= \tilde{w}_n + w'_n - \theta_{\text{tilt}}(\tilde{u}_n + u'_n), \end{aligned} \tag{C1}$$

where $\tilde{u}_n$ and $\tilde{w}_n$ are the wave orbital velocities at sensor n and θ_{tilt} is the sensor tilt relative to the vertical that are used to correct leakage between flow components (Elgar et al. 2005). Tilts are assumed identical for the two sensors (mounted on the same pipe).

The cross-shore and vertical wave bias, ΔU_{12} and ΔW_{12}, in the filtered turbulence fluctuation time series is

$$\begin{aligned} \Delta U_{12} &= -\delta_u \Delta\widetilde{u}_1 + \theta_{\text{tilt}}\widetilde{w}_1 \\ \Delta W_{12} &= -\delta_w \Delta\widetilde{w}_1 - \theta_{\text{tilt}}\widetilde{u}_1, \end{aligned} \tag{C2}$$

where δ_u and δ_w are the ratios of the wave residuals in the adaptive filtering technique to those in the differencing technique (Trowbridge 1998) and $\Delta\widetilde{u}_1$ and $\Delta\widetilde{w}_1$ are the differences of the wave signals measured by the two sensors (Feddersen and Williams 2007). Retaining the first order of θ_{tilt}, the wave biases for the normal stresses $\overline{u'^2}$ and $\overline{w'^2}$ are

$$\overline{\Delta U_{12}\Delta U_{12}} = \delta_u^2 \overline{\Delta\widetilde{u}_1 \Delta\widetilde{u}_1} - 2\delta_u \theta_{\text{tilt}} \overline{\Delta\widetilde{u}_1 \widetilde{w}_1} \tag{C3}$$

and

$$\overline{\Delta W_{12}\Delta W_{12}} = \delta_w^2 \overline{\Delta\widetilde{w}_1 \Delta\widetilde{w}_1} + 2\delta_w \theta_{\text{tilt}} \overline{\Delta\widetilde{w}_1 \widetilde{u}_1}, \tag{C4}$$

respectively. Approximating differences in the wave signals as (Feddersen and Williams 2007)

$$\begin{aligned} \Delta\widetilde{u}_1 &= \frac{\Delta z}{z}(\kappa_w z)^2 \widetilde{u}_1 \\ \Delta\widetilde{w}_1 &= \frac{\Delta z}{z}\widetilde{w}_1, \end{aligned} \tag{C5}$$

where κ_w is a characteristic wavenumber associated with the dominant sea-swell frequency, z is the elevation of the sensor above the bottom, and Δz is the vertical separation of sensors; Eqs. (C3) and (C4) give

$$\begin{aligned} \overline{\Delta U_{12}\Delta U_{12}} &= \delta_u^2 \left(\frac{\Delta z}{z}\right)^2 (\kappa_w z)^4 \sigma_u^2 - 2\delta_u \theta_1 \left(\frac{\Delta z}{z}\right)(\kappa_w z)^2 \overline{\widetilde{u}_1 \widetilde{w}_1} \\ \overline{\Delta W_{12}\Delta W_{12}} &= \delta_w^2 \left(\frac{\Delta z}{z}\right)^2 \sigma_w^2 + 2\delta_w \theta_1 \left(\frac{\Delta z}{z}\right) \overline{\widetilde{u}_1 \widetilde{w}_1}. \end{aligned} \tag{C6}$$

REFERENCES

Aagaard, T., and M. G. Hughes, 2010: Breaker turbulence and sediment suspension in the surf zone. *Mar. Geol.*, **271**, 250–259, https://doi.org/10.1016/j.margeo.2010.02.019.

Ali, N., N. Hamilton, G. Cortina, M. Calaf, and R. B. Cal, 2018: Anisotropy stress invariants of thermally stratified wind turbine array boundary layers using large eddy simulations. *J. Renewable Sustainable Energy*, **10**, 013301, https://doi.org/10.1063/1.5016977.

Apotsos, A., B. Raubenheimer, S. Elgar, R. T. Guza, and J. A. Smith, 2007: Effects of wave rollers and bottom stress on wave setup. *J. Geophys. Res.*, **112**, C02003, https://doi.org/10.1029/2006JC003549.

Ballouz, J. G., and N. T. Ouellette, 2018: Tensor geometry in the turbulent cascade. *J. Fluid Mech.*, **835**, 1048–1064, https://doi.org/10.1017/jfm.2017.802.

Banerjee, S., R. Krahl, F. Durst, and C. Zenger, 2007: Presentation of anisotropy properties of turbulence, invariants versus eigenvalue approaches. *J. Turbul.*, **8**, N32, https://doi.org/10.1080/14685240701506896.

Benilov, A. Y., and B. Filyushkin, 1970: Application of methods of linear filtration to an analysis of fluctuations in the surface layer of the sea. *Izv., Acad. Sci., USSR, Atmos. Oceanic Phys.*, **68**, 810–819.

Bian, C., Z. Liu, Y. Huang, L. Zhao, and W. Jiang, 2018: On estimating turbulent Reynolds stress in wavy aquatic environment. *J. Geophys. Res. Oceans*, **123**, 3060–3071, https://doi.org/10.1002/2017JC013230.

Biferale, L., and I. Procaccia, 2005: Anisotropy in turbulent flows and in turbulent transport. *Phys. Rep.*, **414**, 43–164, https://doi.org/10.1016/j.physrep.2005.04.001.

Boers, M., 2005: Surfzone turbulence. Ph.D. thesis, Delft University of Technology, 171 pp.

Boussinesq, J., 1877: Essai sur la Théorie des Eaux Courantes. Imprimerie Nationale Tech. Doc., 722 pp., https://gallica.bnf.fr/ark:/12148/bpt6k56673076.texteImage.

Bricker, J. D., and S. G. Monismith, 2007: Spectral wave–turbulence decomposition. *J. Atmos. Oceanic Technol.*, **24**, 1479–1487, https://doi.org/10.1175/JTECH2066.1.

Chávez-Dorado, J., I. Scherl, and M. DiBenedetto, 2024: Wave and turbulence separation using dynamic mode decomposition. arXiv, 2403.00223v2, https://doi.org/10.48550/arXiv.2403.00223.

Chen, J., B. Raubenheimer, and S. Elgar, 2024a: Anisotropy of surfzone turbulence. Zenodo, accessed 21 July 2025, https://doi.org/10.5281/zenodo.13737274.

——, ——, and ——, 2024b: Wave and roller transformation over barred bathymetry. *J. Geophys. Res. Oceans*, **129**, e2023JC020413, https://doi.org/10.1029/2023JC020413.

Deigaard, R., and J. Fredsøe, 1989: Shear stress distribution in dissipative water waves. *Coastal Eng.*, **13**, 357–378, https://doi.org/10.1016/0378-3839(89)90042-2.

De Vriend, H. J., and M. J. F. Stive, 1987: Quasi-3D modelling of nearshore currents. *Coastal Eng.*, **11**, 565–601, https://doi.org/10.1016/0378-3839(87)90027-5.

Elgar, S., B. Raubenheimer, and R. T. Guza, 2001: Current meter performance in the surf zone. *J. Atmos. Oceanic Technol.*, **18**, 1735–1746, https://doi.org/10.1175/1520-0426(2001)018<1735:CMPITS>2.0.CO;2.

——, ——, and ——, 2005: Quality control of acoustic Doppler velocimeter data in the surfzone. *Meas. Sci. Technol.*, **16**, 1889, https://doi.org/10.1088/0957-0233/16/10/002.

Feddersen, F., 2010: Quality controlling surf zone acoustic Doppler velocimeter observations to estimate the turbulent dissipation rate. *J. Atmos. Oceanic Technol.*, **27**, 2039–2055, https://doi.org/10.1175/2010JTECHO783.1.

——, 2012: Scaling surf zone turbulence. *Geophys. Res. Lett.*, **39**, L18613, https://doi.org/10.1029/2012GL052970.

——, and A. J. Williams III, 2007: Direct estimation of the Reynolds stress vertical structure in the nearshore. *J. Atmos. Oceanic Technol.*, **24**, 102–116, https://doi.org/10.1175/JTECH1953.1.

——, J. H. Trowbridge, and A. J. Williams III, 2007: Vertical structure of dissipation in the nearshore. *J. Phys. Oceanogr.*, **37**, 1764–1777, https://doi.org/10.1175/JPO3098.1.

George, R., R. E. Flick, and R. T. Guza, 1994: Observations of turbulence in the surf zone. *J. Geophys. Res.*, **99**, 801–810, https://doi.org/10.1029/93JC02717.

Huang, N. E., and Z. Wu, 2008: A review on Hilbert-Huang transform: Method and its applications to geophysical studies. *Rev. Geophys.*, **46**, RG2006, https://doi.org/10.1029/2007RG000228.

Kuik, A. J., G. P. van Vledder, and L. Holthuijsen, 1988: A method for the routine analysis of pitch-and-roll buoy wave data. *J. Phys. Oceanogr.*, **18**, 1020–1034, https://doi.org/10.1175/1520-0485(1988)018<1020:AMFTRA>2.0.CO;2.

Larsen, B. E., and D. R. Fuhrman, 2018: On the over-production of turbulence beneath surface waves in Reynolds-averaged Navier–Stokes models. *J. Fluid Mech.*, **853**, 419–460, https://doi.org/10.1017/jfm.2018.577.

——, D. A. van der A, J. van der Zanden, G. Ruessink, and D. R. Fuhrman, 2020: Stabilized RANS simulation of surf zone kinematics and boundary layer processes beneath large-scale plunging waves over a breaker bar. *Ocean Modell.*, **155**, 101705, https://doi.org/10.1016/j.ocemod.2020.101705.

Launder, B. E., and B. I. Sharma, 1974: Application of the energy-dissipation model of turbulence to the calculation of flow near a spinning disc. *Lett. Heat Mass Transfer*, **1**, 131–137, https://doi.org/10.1016/0094-4548(74)90150-7.

Li, Q., and B. Fox-Kemper, 2020: Anisotropy of Langmuir turbulence and the Langmuir-enhanced mixed layer entrainment. *Phys. Rev. Fluids*, **5**, 013803, https://doi.org/10.1103/PhysRevFluids.5.013803.

Li, Y., B. E. Larsen, and D. R. Fuhrman, 2022: Reynolds stress turbulence modelling of surf zone breaking waves. *J. Fluid Mech.*, **937**, A7, https://doi.org/10.1017/jfm.2022.92.

Lumley, J. L., 1978: Computational modeling of turbulent flows. *Adv. Appl. Mech.*, **18**, 123–176, https://doi.org/10.1016/S0065-2156(08)70266-7.

——, and E. A. Terray, 1983: Kinematics of turbulence convected by a random wave field. *J. Phys. Oceanogr.*, **13**, 2000–2007, https://doi.org/10.1175/1520-0485(1983)013<2000:KOTCBA>2.0.CO;2.

McCaffrey, K., B. Fox-Kemper, P. E. Hamlington, and J. Thomson, 2015: Characterization of turbulence anisotropy, coherence, and intermittency at a prospective tidal energy site: Observational data analysis. *Renewable Energy*, **76**, 441–453, https://doi.org/10.1016/j.renene.2014.11.063.

Mellor, G., 2013: Pressure–slope momentum transfer in ocean surface boundary layers coupled with gravity waves. *J. Phys. Oceanogr.*, **43**, 2173–2184, https://doi.org/10.1175/JPO-D-13-068.1.

Mellor, G. L., and T. Yamada, 1982: Development of a turbulence closure model for geophysical fluid problems. *Rev. Geophys.*, **20**, 851–875, https://doi.org/10.1029/RG020i004p00851.

Mori, N., T. Suzuki, and S. Kakuno, 2007: Noise of acoustic Doppler velocimeter data in bubbly flows. *J. Eng. Mech.*, **133**, 122–125, https://doi.org/10.1061/(ASCE)0733-9399(2007)133:1(122).

Na, B., K.-A. Chang, Z.-C. Huang, and H.-J. Lim, 2016: Turbulent flow field and air entrainment in laboratory plunging breaking waves. *J. Geophys. Res. Oceans*, **121**, 2980–3009, https://doi.org/10.1002/2015JC011377.

——, ——, and H.-J. Lim, 2020: Flow kinematics and air entrainment under laboratory spilling breaking waves. *J. Fluid Mech.*, **882**, A15, https://doi.org/10.1017/jfm.2019.817.

Nadaoka, K., S. Ueno, and T. Igarashi 1988: Sediment suspension due to large scale eddies in the surf zone. *Proc. 21st Int. Conf. Coastal Eng., 1988*, Torremolinos, Spain, ASCE, 1646–1660, https://doi.org/10.1061/9780872626874.123.

Nairn, R. B., J. A. Roelvink, and H. N. Southgate, 1990: Transition zone width and implications for modelling surfzone hydrodynamics. *Coastal Eng. Proc.*, Delft, The Netherlands, ASCE, 68–81, https://doi.org/10.1061/9780872627765.007.

NOAA, 2024: NOAA field data, station no. 8651370. Accessed 9 September 2024, https://tidesandcurrents.noaa.gov/stationhome.html?id=8651370.

Pope, S. B., 2000: *Turbulent Flows*. Cambridge University Press, 771 pp.

Roelvink, J., and M. J. F. Stive, 1989: Bar-generating cross-shore flow mechanisms on a beach. *J. Geophys. Res.*, **94**, 4785–4800, https://doi.org/10.1029/JC094iC04p04785.

Rosman, J. H., and G. P. Gerbi, 2017: Interpreting fixed-location observations of turbulence advected by waves: Insights from spectral models. *J. Phys. Oceanogr.*, **47**, 909–931, https://doi.org/10.1175/JPO-D-15-0249.1.

Ruessink, B. G., 2010: Observations of turbulence within a natural surf zone. *J. Phys. Oceanogr.*, **40**, 2696–2712, https://doi.org/10.1175/2010JPO4466.1.

Scott, C. P., D. T. Cox, T. B. Maddux, and J. W. Long, 2005: Large-scale laboratory observations of turbulence on a fixed barred beach. *Meas. Sci. Technol.*, **16**, 1903, https://doi.org/10.1088/0957-0233/16/10/004.

Shaw, W. J., and J. H. Trowbridge, 2001: The direct estimation of near-bottom turbulent fluxes in the presence of energetic wave motions. *J. Atmos. Oceanic Technol.*, **18**, 1540–1557, https://doi.org/10.1175/1520-0426(2001)018<1540:TDEONB>2.0.CO;2.

Stive, M. J. F., and H. G. Wind, 1982: A study of radiation stress and set-up in the nearshore region. *Coastal Eng.*, **6**, 1–25, https://doi.org/10.1016/0378-3839(82)90012-6.

Svendsen, I. A., 1984: Mass flux and undertow in a surf zone. *Coastal Eng.*, **8**, 347–365, https://doi.org/10.1016/0378-3839(84)90030-9.

——, 1987: Analysis of surf zone turbulence. *J. Geophys. Res.*, **92**, 5115–5124, https://doi.org/10.1029/JC092iC05p05115.

Teixeira, M. A. C., and S. E. Belcher, 2002: On the distortion of turbulence by a progressive surface wave. *J. Fluid Mech.*, **458**, 229–267, https://doi.org/10.1017/S0022112002007838.

Tennekes, H., and J. L. Lumley, 1972: *A First Course in Turbulence*. The MIT Press, 300 pp.

Thomson, J., B. Polagye, V. Durgesh, and M. C. Richmond, 2012: Measurements of turbulence at two tidal energy sites in Puget Sound, WA. *IEEE J. Oceanic Eng.*, **37**, 363–374, https://doi.org/10.1109/JOE.2012.2191656.

Ting, F. C. K., and J. T. Kirby, 1995: Dynamics of surf-zone turbulence in a strong plunging breaker. *Coastal Eng.*, **24**, 177–204, https://doi.org/10.1016/0378-3839(94)00036-W.

——, and ——, 1996: Dynamics of surf-zone turbulence in a spilling breaker. *Coastal Eng.*, **27**, 131–160, https://doi.org/10.1016/0378-3839(95)00037-2.

Trowbridge, J., and S. Elgar, 2003: Spatial scales of stress-carrying nearshore turbulence. *J. Phys. Oceanogr.*, **33**, 1122–1128, https://doi.org/10.1175/1520-0485(2003)033<1122:SSOSNT>2.0.CO;2.

——, M. Scully, and C. R. Sherwood, 2018: The cospectrum of stress-carrying turbulence in the presence of surface gravity waves. *J. Phys. Oceanogr.*, **48**, 29–44, https://doi.org/10.1175/JPO-D-17-0016.1.

Trowbridge, J. H., 1998: On a technique for measurement of turbulent shear stress in the presence of surface waves. *J. Atmos. Oceanic Technol.*, **15**, 290–298, https://doi.org/10.1175/1520-0426(1998)015<0290:OATFMO>2.0.CO;2.

USACE, 2024: USACE field data. Accessed 9 September 2024, https://chlthredds.erdc.dren.mil/thredds/catalog/frf/catalog.html.

Wilcox, D. C., 2006: *Turbulence Modeling for CFD*. 3rd ed. DCW Industries, 522 pp.

Yoon, H.-D., and D. T. Cox, 2010: Large-scale laboratory observations of wave breaking turbulence over an evolving beach. *J. Geophys. Res.*, **115**, C10007, https://doi.org/10.1029/2009JC005748.